

Supramolecular Liquid Crystal Elastomer Adhesives: Role of Internal Damping and Hydrogen Bonding

Subi Choi and Suk-kyun Ahn*

Liquid crystal elastomers (LCEs) have attracted attention as materials for pressure-sensitive adhesives (PSAs) owing to their high internal damping resulting from mesogen reorientation. However, the roles that mesogen reorientation and interfacial interactions play in overall adhesion remain unclear. In this study, a series of supramolecular LCE-based PSAs are prepared by systematically varying the liquid crystal (LC) content and hydrogen bond (H-bond) density to investigate their effects on internal damping, soft elasticity, and adhesion strength. A decreased LC content of the PSAs reduces both internal damping and soft elasticity, resulting in weaker adhesion. When H-bonds are introduced using non-mesogenic monomers in the rigid segment, the mesogen reorientation is restricted, thereby decreasing adhesion. In contrast, incorporating H-bonds into the chain extender (or soft segment) of the supramolecular LCEs improves the adhesion strength with increasing H-bond density, provided the LC content is high. Therefore, the adhesion of supramolecular LCEs is primarily governed by internal damping rather than by H-bond interactions. Moreover, solvent vapor annealing enables reversible adhesion in the supramolecular LCEs by transiently weakening H-bonds and improving surface contact. The non-thermal approach demonstrated in this study yields LCE-based PSAs for heat-sensitive applications such as medical adhesives, skin patches, and semiconductor processing.

viscoelasticity, typically defined by the Dahlquist criterion ($G' < 0.1$ MPa at 1 Hz and 25 °C).^[3,4] This low modulus promotes contact with the substrate and facilitates fibril formation during peeling, thereby enhancing energy dissipation and adhesion. However, excessively viscous behavior can compromise the shear resistance and result in cohesive failure. Therefore, achieving a balance between viscous and elastic responses is essential and requires careful design of polymer networks.

Liquid crystal elastomers (LCEs) are loosely crosslinked anisotropic rubbers comprising rigid mesogenic moieties. Owing to their unique viscoelastic properties, LCEs have recently emerged as a promising class of PSAs.^[5–16] When subjected to stress, the mesogenic domains reorient along the direction of deformation, producing “soft elasticity” behavior, characterized by an extended stress plateau where director rotation occurs without resistance.^[17–22] This behavior enables efficient mechanical energy dissipation during stretching or peeling, resulting in robust adhesion. The unique energy dissipation characteristics

of LCEs are also assessed using dynamic mechanical analysis (DMA). In addition to the primary $\tan \delta$ peak associated with their glass transition temperature (T_g), LCEs typically exhibit a secondary peak or shoulder at temperatures above T_g , which reflects internal damping arising from the rotation of mesogenic domains.^[13,23–29]

Pioneering work on LCE-based PSAs was reported by Terentjev research group in 2019, highlighting the bulk dynamic mechanical response of LCEs and switchable adhesion with temperature.^[5] Several studies on LCE-based PSAs have recently focused on the effects of crosslinking density, the T_g , soft elasticity, and the alignment of LCEs on adhesion strength.^[7–12] The same research group systematically investigated the adhesion mechanism of thermally annealed LCEs with varying crosslinking densities using different adhesion tests, including peel, probe tack, and shear tests.^[8] They also explored the strong, reversible, and heat-activated adhesion of LCEs by tuning the T_g with various primary amine chain extenders.^[12] Cai research group showed that the strong rate-dependent soft elasticity of LCEs improves adhesion better than isotropic PSAs.^[9] They also demonstrated strong adhesion to rough substrates using probe tack and nanoindentation tests, owing to the soft elasticity and

1. Introduction

Pressure-sensitive adhesives (PSAs) are soft viscoelastic materials that adhere to surfaces under light pressure.^[1,2] For effective adhesion, PSAs must exhibit a certain level of liquid-like

S. Choi, S.-k. Ahn
School of Chemical Engineering
Pusan National University
Busan 46241, Republic of Korea
E-mail: skahn@pusan.ac.kr

S.-k. Ahn
Department of Polymer Science and Engineering
Pusan National University
Busan 46241, Republic of Korea

The ORCID identification number(s) for the author(s) of this article can be found under <https://doi.org/10.1002/adfm.202511426>

© 2025 The Author(s). Advanced Functional Materials published by Wiley-VCH GmbH. This is an open access article under the terms of the Creative Commons Attribution License, which permits use, distribution and reproduction in any medium, provided the original work is properly cited.

DOI: 10.1002/adfm.202511426

low crosslinking density of LCEs.^[11] Moreover, White and Hayward demonstrated directional adhesion based on the anisotropic mechanical responses of surface-aligned LCEs.^[10] Recently, we reported a unique approach to maximize internal damping by incorporating slidable polyrotaxane crosslinkers, resulting in enhanced adhesion in LCEs.^[13] Although internal damping and soft elasticity contribute to LCE adhesion, few studies have systematically examined how these properties affect adhesion strength across diverse LCE-based PSAs. For example, LCEs with integrated hydrogen bonds (H-bonds) can reinforce both cohesion and adhesion, as demonstrated in various supramolecular polymer adhesives.^[30–32]

In this study, we systematically varied the LC content and H-bond density in a series of supramolecular LCE adhesives to examine their effects on internal damping, soft elasticity, and adhesion strength. Our findings reveal that adhesion in supramolecular LCEs was primarily governed by intrinsic energy dissipation rather than H-bonding interactions. Interestingly, supramolecular LCEs with high LC content and H-bond density exhibited a synergistic enhancement in adhesion strength during the peel tests. Importantly, we demonstrate a new strategy to achieve reversible adhesion in supramolecular LCEs using solvent vapor annealing. This non-thermal approach enables the dynamic control of adhesion strength for applying LCE-based PSAs in heat-sensitive environments, such as human skin.

2. Results and Discussion

2.1. Material Design for LCE-Based PSAs

We investigated the effects of internal damping and H-bond interactions on the adhesion strength of supramolecular LCEs (Scheme 1a). To examine both the independent and synergistic effects of LC content and H-bond interactions on viscoelastic and adhesion properties, three distinct series of acrylic PSAs were designed by incorporating various secondary components, either non-mesogenic and/or H-bonds, into the LCE network (Scheme 1b). A non-mesogenic monomer lacking H-bonding capability [bisphenol A ethoxylate diacrylate (BE)] was used to selectively vary the LC content in the LCE. Conversely, a non-mesogenic monomer with H-bonding capability [bisphenol A glycerolate (1 glycerol/phenol) diacrylate (BG)] that simultaneously decreased the LC content and increased the H-bond density within the rigid backbone was introduced into the LCE network. Finally, 4-amino-1-butanol (AB) was employed as a flexible chain extender to introduce H-bonding into the soft segment while preserving the overall LC content.

In the PSA series, the molar ratio of the secondary components (BE, BG, and AB; y) was varied from 0 to 100 mol%, with the LC monomer (RM82) and *n*-hexylamine ratio (x) adjusted accordingly ($y = 100 - x$). Each PSA series is denoted as BE(y/z), BG(y/z), and AB(y/z), where y is the mol% of the secondary components and z is the overall LC weight percentage (wt%) in the PSA.

2.2. Synthesis and Thermal Properties

To prepare the PSAs, a mixture of diacrylate monomers (BE/RM82, BG/RM82, and RM82) first underwent chain exten-

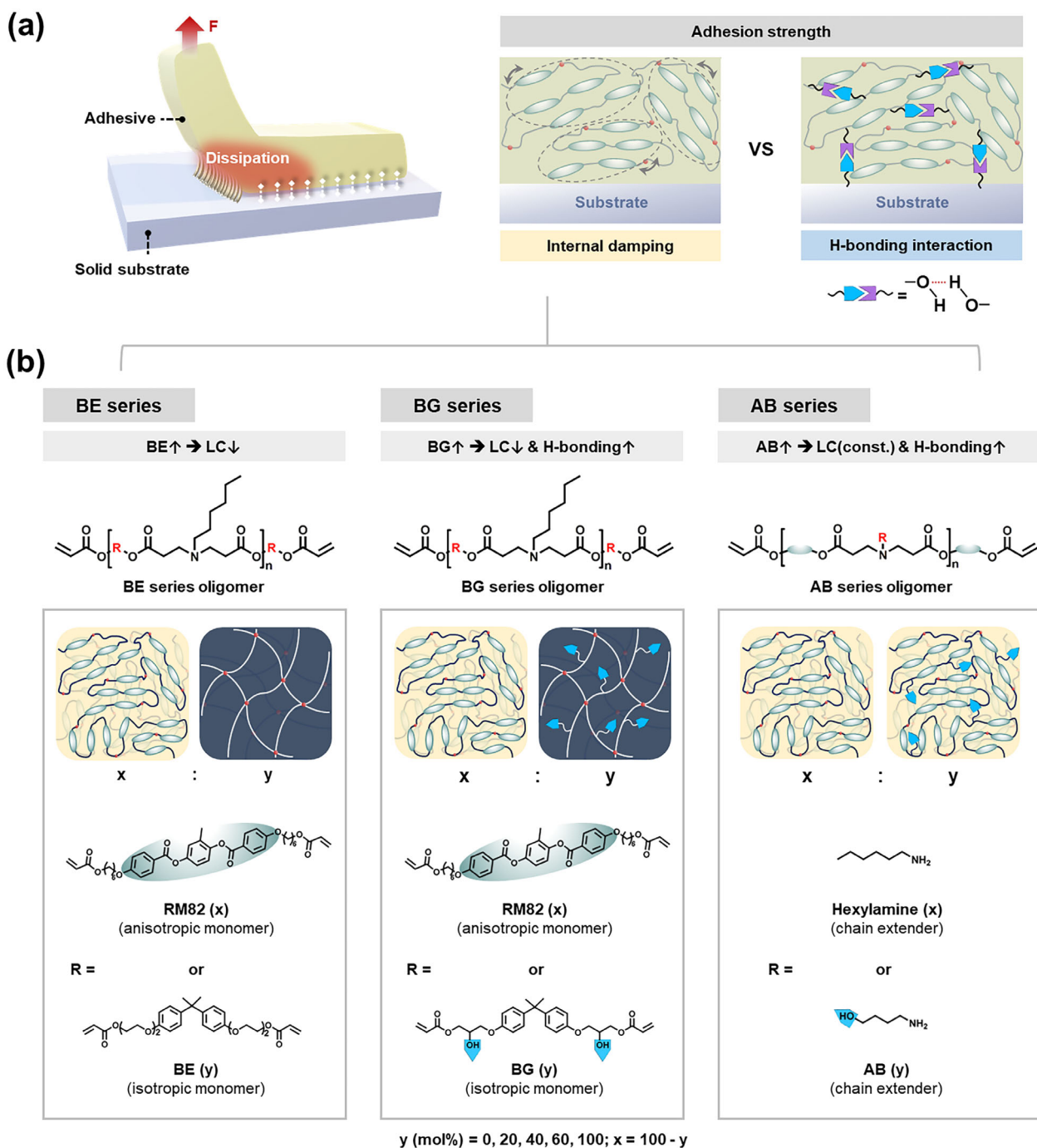
sion with primary amine chain extenders (*n*-hexylamine and/or AB) via an aza-Michael addition-based step-growth reaction for 21 h at 65 °C. The molar ratio of the acrylate and amine functionalities was set to 1.01:1 to ensure the introduction of terminal diacrylate groups in the resulting oligomers. Further synthetic details are described in the experimental section. The prepared oligomers were bar-coated onto a 100- μ m-thick poly(ethylene terephthalate) (PET) backing film at the isotropic temperature. Subsequently, they were photopolymerized at room temperature to produce crosslinked PSAs without a specific molecular alignment (Figure 1a). The gel fraction of all the PSAs was $\approx 80\%$, suggesting the formation of an efficient network within the PSAs (Figure S1 and Table S1, Supporting Information).

The thermal transitions and LC phases of each PSA series were investigated using differential scanning calorimetry (DSC) and polarized optical microscopy (POM). Increasing the content of the non-mesogenic BE component gradually decreased both the nematic-to-isotropic transition temperature (T_{ni}) and associated enthalpy change (ΔH); however, the T_g remained consistent at ≈ -20 °C. The gradual decreases in T_{ni} and ΔH in the BE series were caused by a decreasing LC content with increasing BE concentration (Figure 1b and Table 1). Similar decreases in T_{ni} and ΔH were observed in the BG series with increasing BG content. However, the T_g in the BG series gradually increased from -20 to 3 °C due to restricted segmental mobility arising from stronger H-bonding (Figure 1c). At comparable LC contents (66 and 52 wt.%), the BG series exhibited higher T_{ni} values than the BE series; thus, H-bonding in the BG series enhanced intermolecular cohesion within the LC domain, resulting in a stable nematic phase. Consistent with their higher LC content, pronounced T_{ni} peaks with relatively high ΔH values (≈ 0.5 – 0.8 J g⁻¹) were observed in the AB series (Figure 1d). Both T_g and T_{ni} gradually increased with increasing AB content due to stronger H-bonding within the network. Additionally, we determined the T_g and T_{ni} of the PSA networks by DSC. Although the T_g of each PSA network followed a similar trend to its corresponding oligomer series, the T_{ni} was often unclear or not well-defined in the cross-linked networks (Figure S2, Supporting Information).^[33,34]

The birefringence of the crosslinked PSAs observed using POM showed trends similar to those observed for their thermal properties. In both the BE and BG series, the birefringence became weaker with decreasing LC content and eventually disappeared in the samples with low LC contents (BE(60/36) and BG(60/37)) (Figure 1b,c). In contrast, the AB series maintained strong birefringence across all compositions, indicating a high LC content (Figure 1d). Thus, both the LC content and H-bond density significantly affected the thermal properties and LC phase behavior of the PSAs.

2.3. Characterization of Hydrogen Bonding

Fourier-transform infrared (FT-IR) spectroscopy was conducted for both the BG and AB series to investigate H-bond formation within the supramolecular LCEs. As shown in Figure 2a,d, the O–H stretching vibration peak observed in the 3300–3600 cm⁻¹ region gradually increased in intensity with increasing BG or AB content, indicating the formation of H-bonding. Notably, the BG



Scheme 1. a) Schematic of internal damping and H-bonding interactions as key contributors to adhesion strength in LCE-based PSAs. b) Materials design and corresponding network morphologies of BE, BG, and AB series to investigate the effects of LC content and H-bonding on adhesion.

series exhibited a stronger O–H stretching peak compared with that of the AB series, suggesting a greater extent of H-bonding. The stronger H-bonding in the BG series was attributed to the higher hydroxyl-group density of the BG monomer and H-bond formation within the rigid backbone, unlike the flexible chain extenders in the AB series. Stronger H-bonding in the BG series resulted in higher T_g values than those of the AB series, as observed in DSC results (Figure 1c,d).

H-bonds reversibly dissociate at elevated temperatures and reform upon cooling.^[35] Consistent with this behavior, the intensity of the O–H peak decreased upon heating in both the BG and AB series, indicating thermal dissociation of the H-bonds (Figure S3, Supporting Information). Notably, the BG(60/37) sample exhibited an abrupt decrease in O–H peak intensity at $\approx 180^\circ\text{C}$, indicating the dissociation temperature (T_{disso}) of H-bonds (Figure 2b). This abrupt transition was unique to BG(60/37),

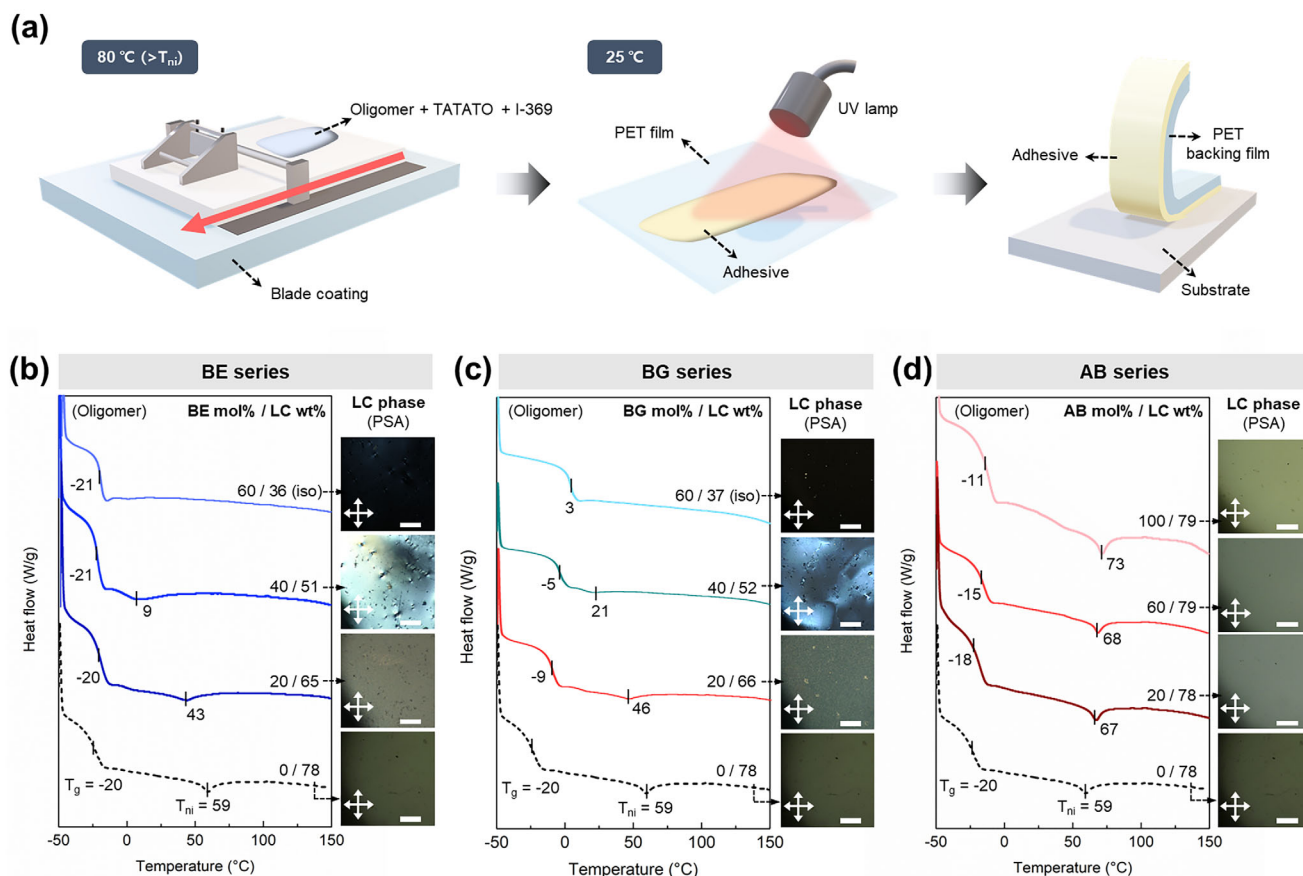


Figure 1. a) Schematic of the fabrication process of PSAs. b–d) DSC thermograms of oligomers obtained during the second heating cycle (left) and POM images of LC phases in each adhesive at room temperature (right). Scale bars in the POM images represent 100 μm.

which exhibited the highest initial O–H peak intensity. In contrast, the AB series exhibited a lower T_{disso} (≈ 120 °C) because H-bonds on the flexible chains were more readily dissociated than those on rigid backbones (Figure 2e).^[36] Upon cooling, the intensity of the O–H peak recovered in both BG(60/37) and AB(100/79), confirming the reversibility of H-bond formation in the supramolecular LCEs (Figure 2c,f).

2.4. Viscoelastic Properties and Temperature-Dependent Deformation

The viscoelastic properties of the PSAs were investigated using DMA. In addition to the primary $\tan \delta$ peak associated with segmental motion (T_g), LCEs can exhibit a secondary $\tan \delta$ peak (or shoulder) at above T_g , associated with the rotation of mesogenic domains. This additional internal dissipation, referred to as internal damping (T_{dm}), is related to the soft elasticity observed in stress-strain curves.

The BE series exhibited a consistent T_g of ≈ 12 °C across all compositions, and T_{dm} appeared between 40 and 60 °C (Figure 3a and Table 1). With increasing BE content, T_{dm} gradually decreased due to the reduced LC content. In the BG series, increasing the BG content resulted in a gradual increase in T_g

driven by stronger H-bonding and reduced internal damping due to the lower LC content (Figure 3b). However, a secondary shoulder was still observed even in the isotropic BG(60/37) sample, likely attributed to energy dissipation from H-bonding.^[35,37,38] As the AB content increased in the AB series, T_g slightly increased (Figure 3c). Simultaneously, the T_{dm} peaks became more pronounced, suggesting greater energy dissipation driven by the synergistic effects of mesogen rotation and H-bonding. All PSA series exhibited comparable rubbery plateaus and moduli (0.1–1.7 MPa) at 130 °C, suggesting efficient network formation with comparable crosslink densities, with results summarized in Table 2. The crosslinking densities (ν_e) of each PSA was estimated from these rubbery moduli according to Equation (1):

$$\nu_e = \frac{E'}{3RT} \quad (1)$$

where E' is the storage modulus at 130 °C, R is the gas constant, and T is the temperature (in Kelvin). The crosslinking densities of all PSA series were determined to be in the range of 1×10^{-5} to 1.7×10^{-4} mol cm⁻³.

Iso-stress measurements were conducted to further examine the effects of H-bonding and internal damping on the temperature-dependent deformation of PSAs. In the iso-stress

Table 1. Thermal and viscoelastic properties of the oligomers and LCEs.

Adhesives			$T_{g/oligomer}$ [°C] ^{a)}	$T_{g/PSA}$ [°C] ^{a)}	$T_{g/PSA}$ [°C] ^{b)}	$T_{ni/oligomer}$ [°C] ^{a)}	$\Delta H_{oligomer}$ [J g ⁻¹] ^{a)}	G [%] ^{c)}
BE series	mol%	LC [wt.%]						
	0	78	−20	−11	12	59	0.48	80
	20	65	−20	−11	12	43	0.38	81
	40	51	−21	−13	11	9	0.13	82
	60	36 (iso)	−21	−15	11	—	—	81
BG series	0	78	−20	−11	12	59	0.48	80
	20	66	−9	−6	21	46	0.43	83
	40	52	−5	−2	26	21	0.2	83
	60	37 (iso)	3	4	26	—	—	83
AB series	0	78	−20	−11	12	59	0.48	80
	20	78	−18	−8	12	67	0.57	81
	60	79	−15	−7	13	68	0.62	79
	100	79	−11	−4	16	73	0.79	79

a) Determined from the second heating DSC curves at a rate of 10 °C min^{−1} under nitrogen; b) Determined from the tan δ curve using DMA at a rate of 3 °C min^{−1}; c) Determined by comparing the mass before and after extraction using DMF as solvent.

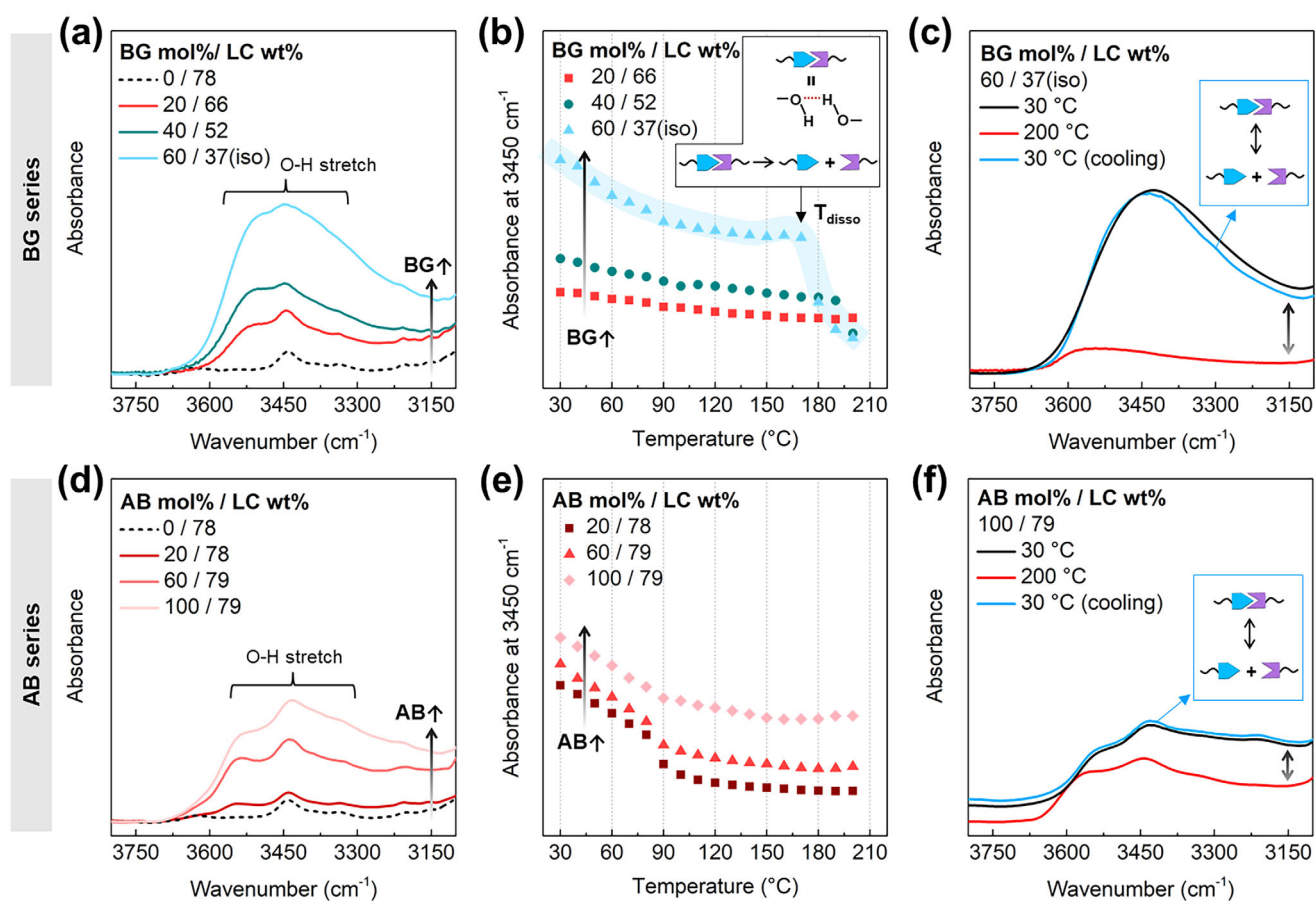


Figure 2. FT-IR spectra of H-bonding in the BG and AB series adhesives. O–H stretching peaks (3600–3100 cm^{−1}) as a function of H-bonding in a) BG and d) AB series adhesives. Temperature-dependent dissociation of H-bonds in b) BG and e) AB series adhesives. Reversible dissociation and reformation of H-bonds in c) BG(60/37) and f) AB(100/79) adhesives.

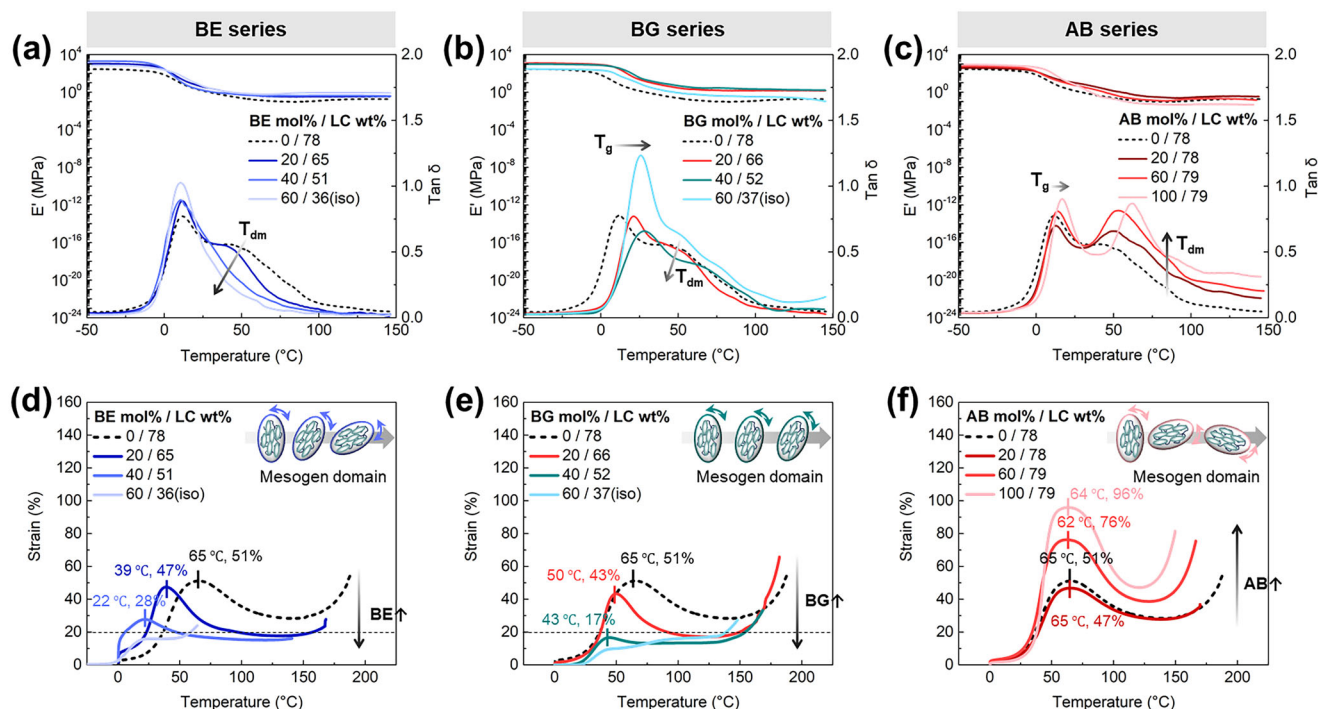


Figure 3. Storage modulus and $\tan \delta$ curves of the PSA series during temperature ramping in DMA: a) BE, b) BG, and c) AB series. Iso-stress curves of the PSA series under constant stress conditions obtained using DMA: d) BE, e) BG, and f) AB series.

heating curve, LCEs can undergo network alignment along the loading direction and spontaneously contract upon reaching the isotropic phase, producing a peak at T_{mi} .^[39–41] The maximum strain induced by the stress alignment directly reflects the ability of the mesogenic domains to reorient, representing soft elasticity. In both the BE and BG series, the maximum strain decreased with decreasing LC content (Figure 3d,e). Notably, the BG series exhibited a lower maximum strain than the BE series at comparable LC contents, suggesting that the H-bonds

within the rigid segments limited mesogen reorientation. In contrast, the AB series exhibited a gradual increase in maximum strain with increasing AB content, consistent with the enhanced T_{dm} peak observed in the $\tan \delta$ curves (Figure 3c,f). Unlike the strongly bound H-bonds in the BG series, the loosely bound H-bonds within the flexible chain extenders in the AB series did not hinder mesogen reorientation. Instead, these H-bonds promoted energy dissipation and enhanced the mechanical toughness of the supramolecular LCEs.

Table 2. Rubbery modulus and corresponding crosslinking densities of LCEs.

Adhesives	Rubbery modulus at 130 °C [MPa] ^{a)}		Crosslinking density at 130 °C [mol cm ⁻³] ^{a)}	
BE series	mol%	LC [wt.%]		
	0	78	0.2	2×10^{-5}
	20	65	0.4	4×10^{-5}
	40	51	0.9	9×10^{-5}
	60	36 (iso)	1	10×10^{-5}
BG series	mol%	LC [wt.%]		
	0	78	0.2	2×10^{-5}
	20	66	1.5	1.5×10^{-4}
	40	52	1.7	1.7×10^{-4}
	60	37 (iso)	0.2	2×10^{-5}
AB series	mol%	LC [wt.%]		
	0	78	0.2	2×10^{-5}
	20	78	0.4	4×10^{-5}
	60	79	0.2	2×10^{-5}
	100	79	0.1	1×10^{-5}

^{a)} Determined from the storage modulus using DMA at a rate of 3 °C min⁻¹.

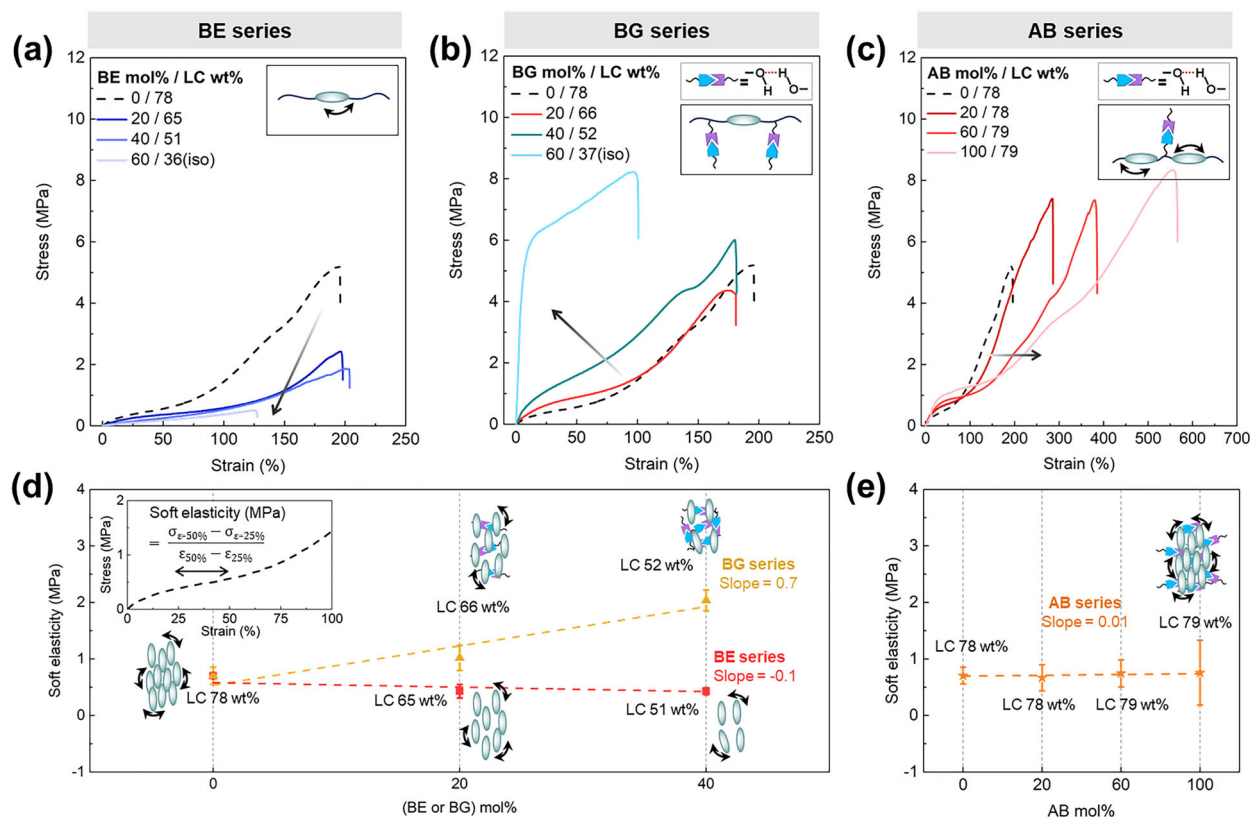


Figure 4. Stress–strain curves of the PSA series obtained using the UTM: a) BE, b) BG, and c) AB series. Soft elasticity quantified from stress differences between 25% and 50% strain: d) BE, BG, and e) AB series.

2.5. Mechanical Properties and Soft Elasticity

The mechanical properties and soft elasticity of PSAs were examined using uniaxial tensile test, with results shown in **Figure 4** and summarized in **Table 3**. Increasing the BE content gradually

decreased both the elastic modulus and mechanical toughness (**Figure 4a**; **Figure S4a**; Supporting Information). In contrast, increasing the BG content enhanced both the elastic modulus and toughness through network reinforcement via H-bonding (**Figure 4b**; **Figure S4b**, Supporting Information). The AB series

Table 3. Mechanical properties of the LCEs.

Adhesives	mol%	LC [wt.%]	Elastic modulus [MPa] ^{a)}	Strain [%] ^{a)}	Tensile strength [MPa] ^{a)}	Toughness [MJ m ⁻³] ^{a)}	Soft elasticity [MPa] ^{b)}
BE series	0	78	2.5 ± 1	196 ± 36	5 ± 0.5	4 ± 1	0.7 ± 0.1
	20	65	2 ± 0.5	198 ± 10	2 ± 0.5	2 ± 0.2	0.4 ± 0.1
	40	51	0.7 ± 0.25	204 ± 23	2 ± 0.7	1.5 ± 0.5	0.4 ± 0.1
	60	36 (iso)	0.5 ± 0.15	128 ± 16	0.5 ± 0.1	0.3 ± 0.1	–
BG series	0	78	2.5 ± 1	196 ± 36	5 ± 0.5	4 ± 1	0.7 ± 0.1
	20	66	4 ± 0.8	181 ± 42	4 ± 0.3	4 ± 0.7	1 ± 0.2
	40	52	9 ± 2	181 ± 5	6 ± 0.6	5 ± 0.2	2 ± 0.2
	60	37 (iso)	90 ± 28	100 ± 18	8 ± 1	7 ± 1	–
AB series	0	78	2.5 ± 1	196 ± 36	5 ± 0.5	4 ± 1	0.7 ± 0.1
	20	78	4 ± 0.4	287 ± 46	7 ± 0.6	9 ± 2	0.7 ± 0.2
	60	79	5 ± 1	386 ± 69	8 ± 1	11 ± 2	0.7 ± 0.2
	100	79	5 ± 0.4	567 ± 71	9 ± 2	21 ± 2.5	0.8 ± 0.6

^{a)} Determined from the stress-strain curve using UTM at a rate of 100 mm min⁻¹ at room temperature; ^{b)} Calculated from the slope of the stress plateau in the strain range of 25% to 50%.

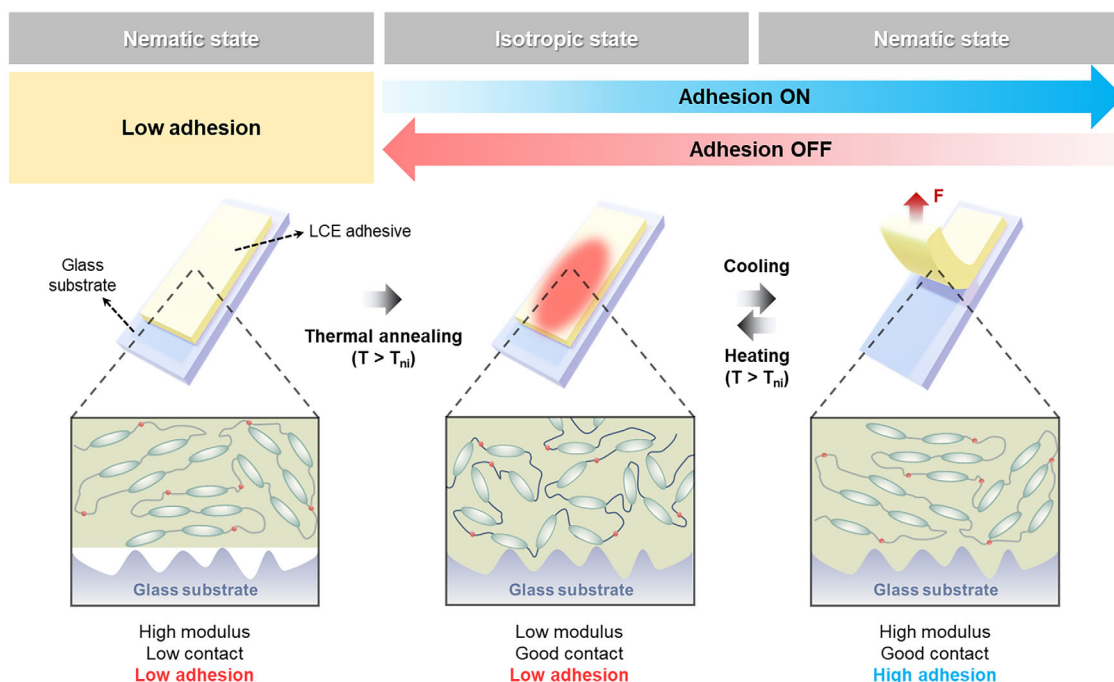


Figure 5. Mechanism of thermally induced adhesion of LCE-based PSAs. After heating to the isotropic phase, the chain mobility increases and enables better contact with the substrate. After cooling back to the nematic phase, the LC ordering recovers with a removal of processing hysteresis, results in strong adhesion. Reheating to the isotropic phase lowers the adhesion, and enables clean detachment.

showed a similar trend; however, because of weaker H-bonding, only a moderate increase in the elastic modulus was observed (Figure 4c; Figure S4c, Supporting Information).

The soft elasticity of the PSAs was influenced by LC content and H-bonding. The stress plateaus progressively shortened with increasing BE or BG content due to the reduced LC content (Figure 4a,b). In contrast, all the AB series exhibited apparent stress plateaus owing to the higher LC content (Figure 4c). In particular, AB(100/79) with the strongest H-bonding capability showed a considerably longer stress plateau, resulting in enhanced toughness (21 MJ m^{-3}). The extended stress plateau and improved toughness of AB(100/79) resulted from H-bond dissociation and reformation during elongation, which promoted efficient energy dissipation and delayed failure.^[42,43] To quantitatively assess the soft elasticity of each PSA series, the slope between 25% and 50% strain was calculated from the stress–strain curves.^[24] The BE series exhibited a negative slope of -0.1 , indicating decreased stress resistance, primarily due to the reduced LC content (Figure 4d). In contrast, the BG series exhibited a steeper positive slope of 0.7 , implying that the strong H-bonded network impeded the rotation of the mesogens. This result was consistent with the iso-stress results (Figure 3e). Conversely, the AB series displayed a nearly flat slope of 0.01 due to the high LC content and relatively weak H-bonds, which enabled greater mesogen rotation (Figure 4e).

2.6. Thermally Induced Adhesion

Although conventional PSAs instantly adhere at room temperature, LCE-based PSAs often require thermal annealing to activate

adhesion.^[8] Upon heating to the isotropic phase, the increased chain mobility facilitated improved contact with the substrate. Upon cooling to the nematic phase, the PSA restored LC ordering without hysteresis, thereby enhancing adhesion (Figure 5).

To compare the peel strengths of the PSA series, 180° peel tests were performed using a DMA equipped with tensile clamps. Each PSA series was first annealed at the isotropic phase, then cooled to room temperature (nematic phase) before testing at a temperature of $T_g + 13^\circ \text{C}$ (Figure 6a). The peel strength is defined as the average force derived from the force–displacement curve (Figure 6b). AB(0/78), which lacked H-bonding, exhibited enhanced adhesion upon annealing at an isotropic temperature (T_{iso}). In contrast, AB(100/79), which has H-bonding capability, demonstrated the highest adhesion after annealing above the T_{disso} (Figure 6c). Thus, the dissociation of H-bonds facilitated improved surface contact. Consequently, all samples were annealed at T_{disso} (150°C) before the peel tests.

Increasing the BE content resulted in a gradual decrease in peel strength as the LC content decreased (Figure 6d), highlighting the importance of the LC content in adhesion. In contrast, the BG series showed two distinct trends (Figure 6e): 1) at high LC contents (52–78 wt.%), the peel strength decreased with increasing BG content, and 2) at low LC contents (37 wt.%), the peel strength increased. Generally, the adhesion strength of LCE-based PSAs is directly associated with their soft elasticity. During debonding, the ability to dissipate mechanical energy is affected by the stress plateau length. For example, a longer stress plateau enables the PSA to withstand more stress, resulting in a higher peel strength. Thus, increasing the content of either BE or BG reduced the LC content, soft elasticity, and peel strength (Figure 4d). The reduction in peel strength was

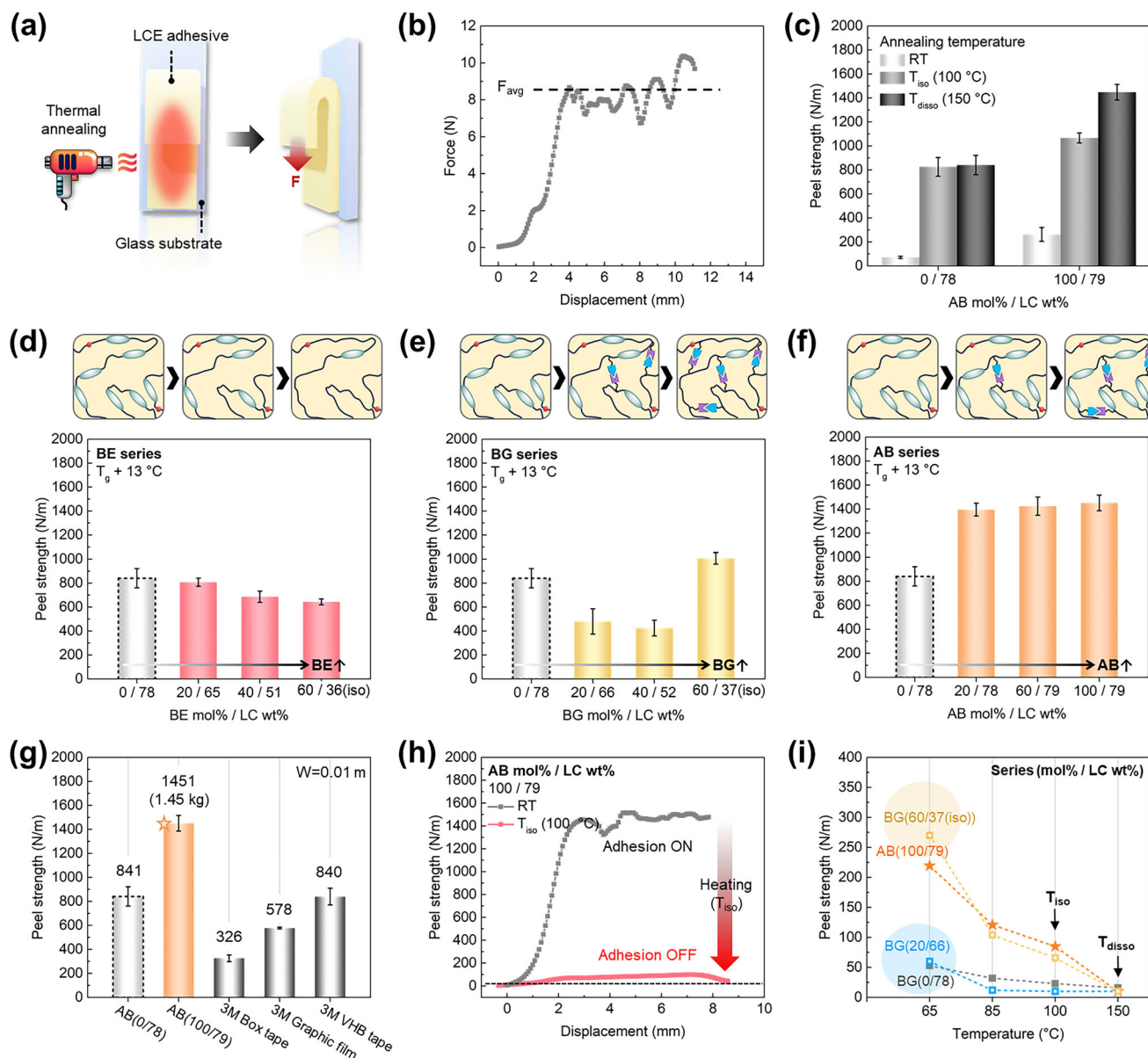


Figure 6. Peel strengths of the PSA series measured in the rubbery state using DMA. a) Schematic of thermally induced adhesion. b) Representative force-displacement curve obtained from the 180° peel test. c) Peel strengths of the AB series PSAs after thermal annealing at room temperature, T_{iso} , and T_{disso} . Peel strengths of d) BE, e) BG, and f) AB series PSAs after annealing. g) Comparison of the AB(100/79) adhesive with commercial PSAs, confirming its superior peel strength. h) Thermally switchable adhesion demonstrated by detachment of the AB(100/79) adhesive upon heating to T_{iso} . i) Temperature-dependent adhesion of BG and AB series PSAs, highlighting distinct detachment behaviors governed by LC content and H-bonding.

more pronounced in the BG series because H-bonding restricted the rotation of mesogens, further decreasing the soft elasticity (Figures 3e and 4d). In contrast, the AB series consistently exhibited high peel strengths across all compositions (Figure 6f) because introducing H-bonding into the flexible chain extenders helped preserve the high LC content and enhanced toughness, resulting in pronounced soft elasticity (Figures 3f and 4c). Therefore, the adhesion of LCE-based PSAs was primarily governed by internal dissipation rather than H-bonding interactions. Notably, the 10 mm-wide AB(100/79) sample outperformed commercial PSAs, supporting up to 1.45 kg (Figure 6g). Moreover, the adhe-

sion strength significantly decreased when heated to T_{iso} , confirming the thermally switchable nature of adhesion (Figure 6h).

Temperature-dependent adhesion was evaluated through 180° peel tests using DMA (Figure 6i; Figure S5, Supporting Information). For BG(20/66), the peel strength decreased to nearly zero at T_{iso} , similar to that of BG(0/78). In contrast, BG(60/37) exhibited a significant decrease only at T_{disso} . Thus, at lower LC contents, the adhesion of PSAs was primarily driven by H-bond interactions. Similarly, the peel strength of AB(100/79) decreased to nearly zero at T_{disso} , highlighting the critical role of H-bonding in both the adhesion and debonding processes.

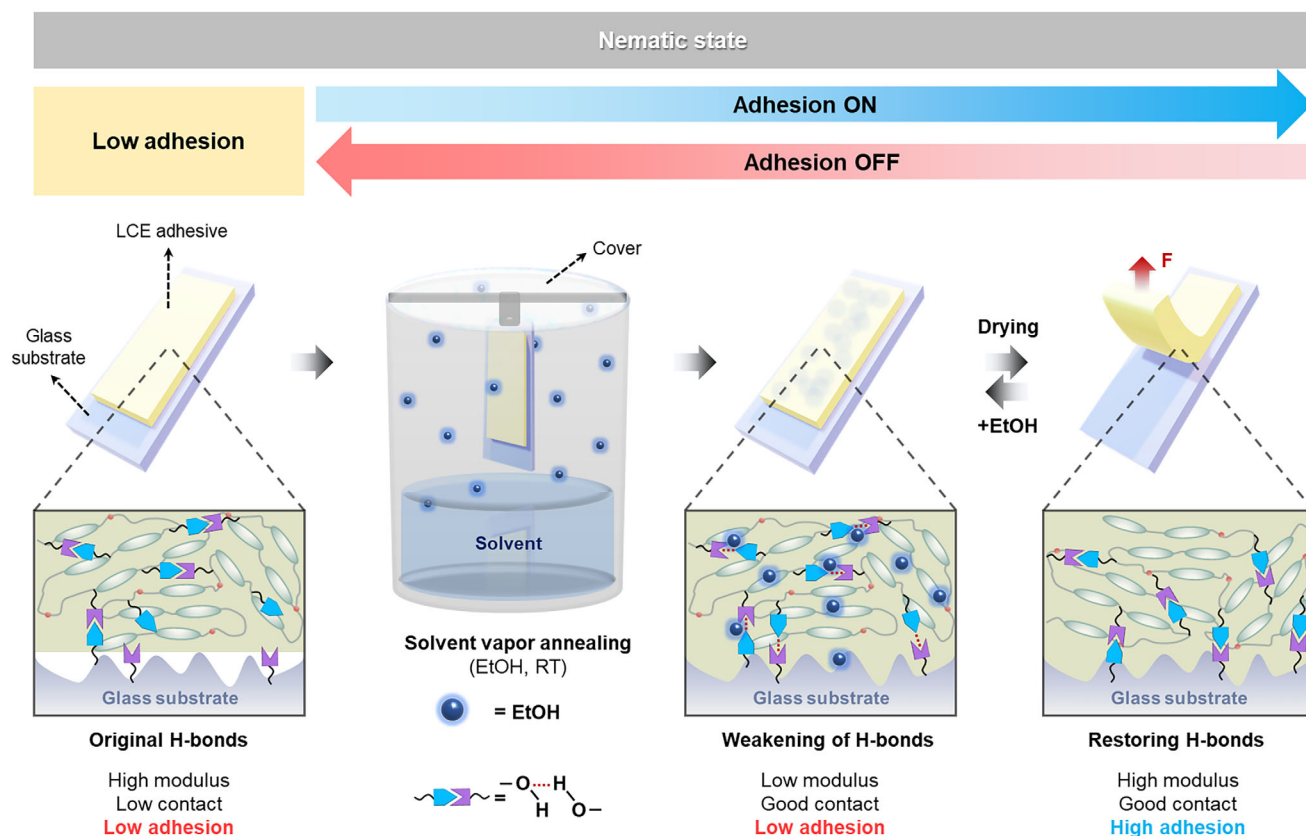


Figure 7. Mechanism of solvent-induced adhesion of supramolecular LCE-based PSAs. Exposure to the solvent vapor enhances chain mobility and weakens H-bonding, thereby increasing surface contact. After solvent removal, H-bonds reform, resulting in strong adhesion. Re-exposure to the solvent vapor facilitates clean detachment by weakening H-bonding.

2.7. Solvent-Induced Adhesion

The LCE-based PSAs exhibited enhanced adhesion after thermal annealing above the T_{ni} . However, their application is limited to heat-sensitive substrates such as electronic components, circuit boards, and human skin.^[8] To address this issue, previous studies introduced non-mesogenic co-monomers or mesogens with weaker π - π interactions into LCE networks.^[5,14,44] While these strategies effectively reduce the annealing temperature, they often weaken the mesogenic contribution, resulting in a lower adhesion strength.

To address these challenges, we introduced solvent vapor annealing to the supramolecular LCE adhesives for reversible adhesion control without heat. Solvent vapor annealing is widely used to control the nanoscale ordering in block copolymers and manipulate the interfacial interactions between organic electronics and substrates.^[45,46] As illustrated in **Figure 7**, PSAs initially attached to the nematic state exhibit low adhesion due to poor surface contact. Upon exposure to the solvent vapor, the H-bonds are temporarily weakened,^[47] thereby improving the surface contact. As the solvent evaporated, the H-bonds are reformed, enhancing adhesion.

FT-IR spectroscopy was used to assess the effects of the solvent on the functional groups. Before testing, freestanding PSA films were prepared without PET backing. The samples

were suspended in a beaker containing ethanol and annealed at room temperature (Figure S6, Supporting Information). After annealing, the samples were dried in a vacuum oven for 1 h at 40 °C. As shown in **Figure 8a,b**, AB(0/78) exhibited no significant changes in the O-H stretching peak following exposure to ethanol. In contrast, AB(100/79) exhibited a significant increase in the O-H stretching peak after 10 min of exposure to the solvent (Figure S9a, Supporting Information). This O-H stretching peak originated from ethanol because it more readily penetrated AB(100/79)-containing hydroxyl groups owing to favorable polar interactions. After drying the ethanol, the O-H stretching peak decreased again. Although all samples slightly changed in weight following solvent vapor annealing, the weight was fully recovered after drying with no visible deformation, thus confirming that the annealing process did not induce structural damage or material loss (Figure S7 and Table S2, Supporting Information).

The storage moduli of the PSAs were evaluated through frequency sweep measurements at 25 °C using DMA. These measurements were conducted within 30 min of solvent vapor annealing, during which solvent evaporation was minimal, with results summarized in Table S3 (Supporting Information). As shown in **Figure 8c,d**, both AB(0/78) and AB(100/79) exhibited reductions in storage moduli following exposure to ethanol. Notably, the storage modulus of AB(100/79) reached ≈ 0.17 MPa at 1 Hz; this value approached the Dahlquist criterion threshold

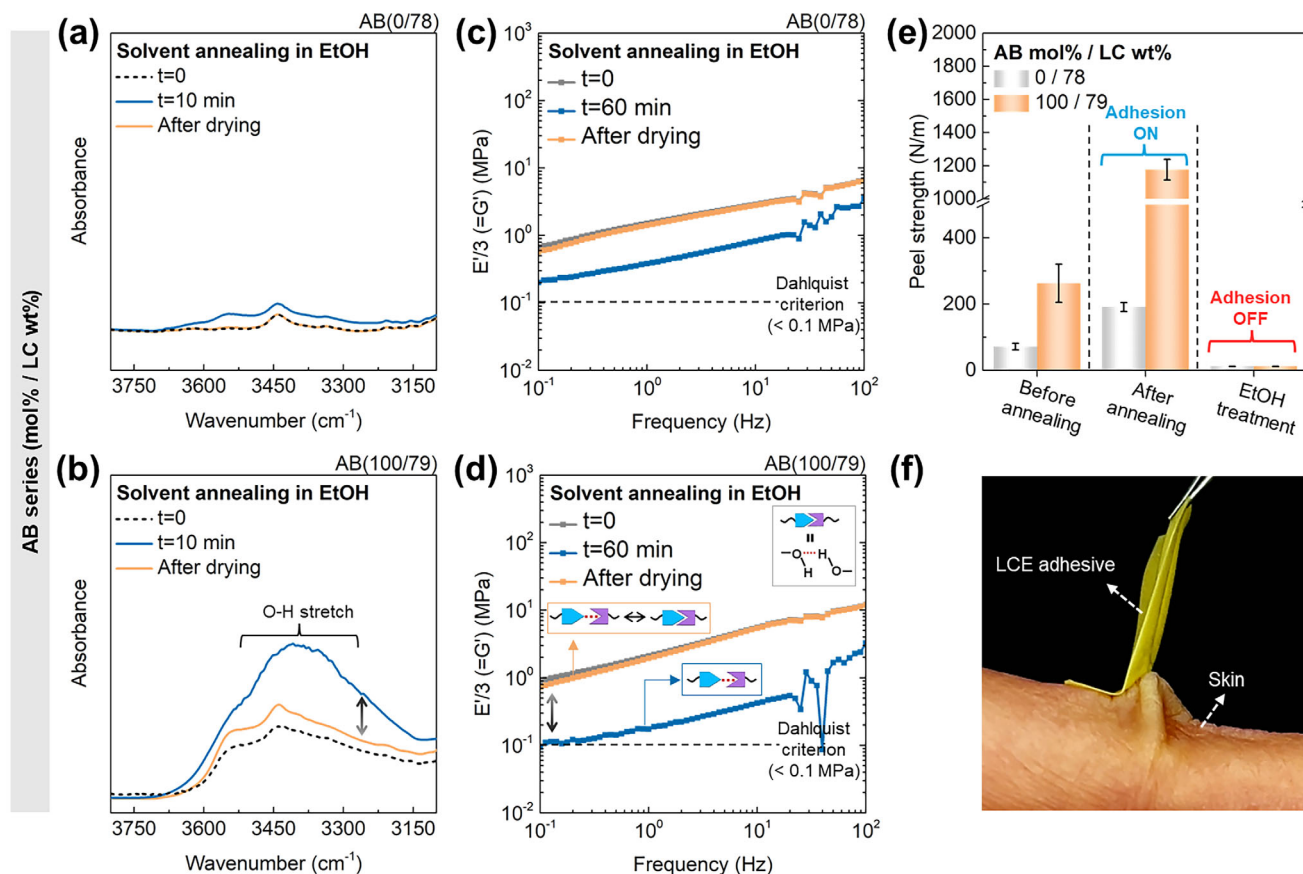


Figure 8. FT-IR spectra of AB series PSAs before and after solvent vapor annealing: a) AB(0/78) and b) AB(100/79). Storage moduli during frequency sweeps at 25 °C: c) AB(0/78) and d) AB(100/79). e) Peel strengths of the AB series PSAs before and after solvent annealing, followed by ethanol treatment, revealing reversible adhesion. f) Demonstration of strong adhesion on skin with the AB(100/79) adhesive.

(<0.1 MPa) for PSA adhesion.^[4] Therefore, the weakening of H-bonds softened the network to improve surface contact. Moreover, the modulus recovered after drying, implying the reformation of H-bonds. Although AB(0/78), which lacked H-bonds, showed a similar trend, the decrease in modulus (≈ 0.38 MPa at 1 Hz) was less than that of AB(100/79).

The peel strengths of the solvent-annealed PSAs were evaluated through 180° peel tests using DMA (Figure 8e). Both the AB(0/78) and AB(100/79) samples exhibited more than a two-fold increase in peel strength following exposure to ethanol, with AB(100/79) exhibiting the highest value (≈ 1200 N m⁻¹) (Movie S1, Supporting Information). This enhancement was attributed to the synergistic effects of the improved surface contact and reformed H-bonding. The slightly lower peel strength compared with that achieved by thermal annealing (≈ 1450 N m⁻¹) was likely due to solvent vapor annealing in the nematic state. Moreover, re-exposure to ethanol vapor decreased the peel strength to nearly zero, confirming complete detachment. Notably, AB(100/79) demonstrated strong adhesion to human skin and enabled clean removal without causing damage (Figure 8f; Movie S2, Supporting Information).

To investigate the effect of solvent quality on solvent-annealed adhesion, AB(0/78) and AB(100/79) samples were treated with various solvents—including isopropanol (IPA), deionized (DI)

water, and acetone—and compared to ethanol-treated samples. These solvents were selected due to their relatively low toxicity. Note that IPA, DI-water, and acetone represent a marginal solvent with H-bonding ability, a poor solvent with H-bonding ability, and a good solvent lacking H-bonding capability, respectively. For the AB(0/78) sample, no significant changes were observed in the O–H stretching peak in the FT-IR spectra after solvent treatment, regardless of solvent type (Figure S8a, Supporting Information). While the storage moduli of solvent-treated AB(0/78) samples decreased due to network softening, the resulting enhancement in peel strength was marginal (Figure S8b,c, Supporting Information). In contrast, the AB(100/79) sample exhibited a marked increase in O–H peak intensity after treatment with IPA and DI water (Figure S9a, Supporting Information). Similar to ethanol, IPA treatment led to a comparable decrease in storage modulus and enhancement in peel strength, although a longer exposure time (2 h) was required due to its higher boiling point (Figure S9b,c, Supporting Information). DI water treatment showed minimal effects on both storage modulus and peel strength, likely due to its poor penetration into the sample. Lastly, acetone treatment reduced the storage modulus through network swelling-induced softening, but resulted in only marginal enhancement in peel strength compared to ethanol or IPA. These results suggest that the enhancement mechanism in peel strength after solvent vapor

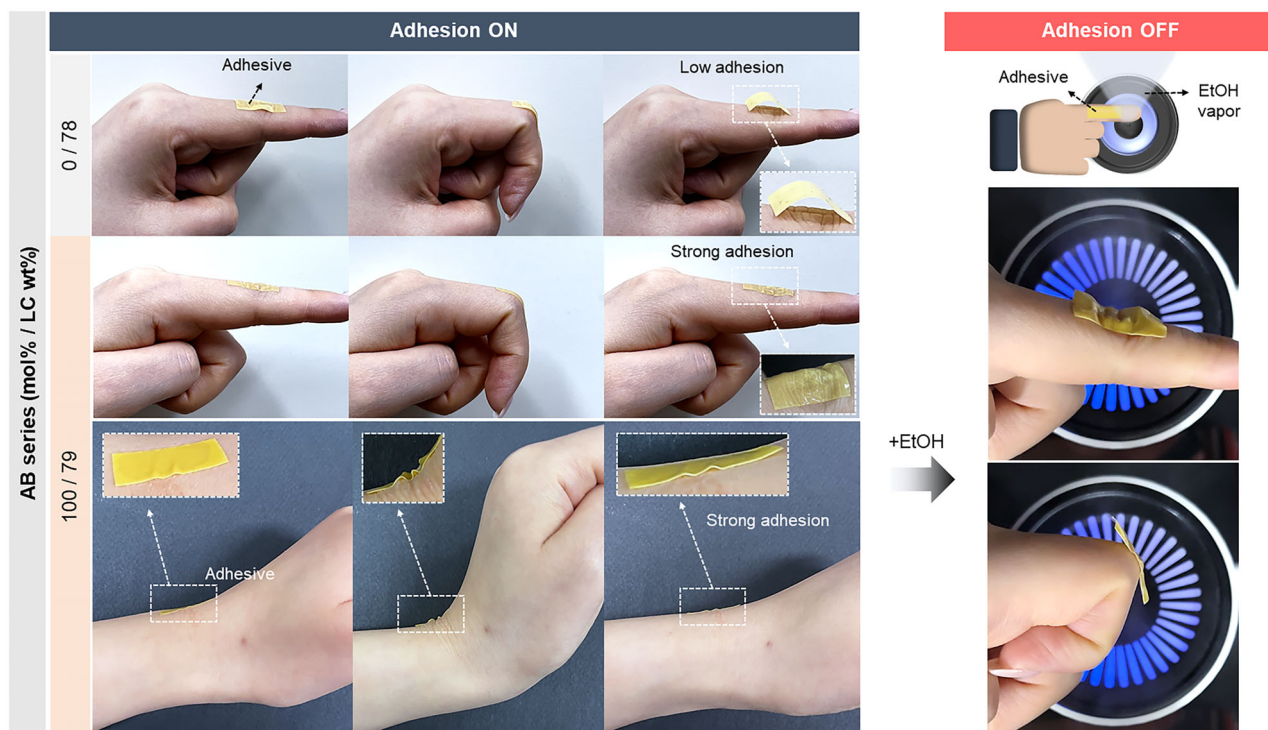


Figure 9. Demonstration of the adhesion and detachment behaviors of the AB series PSAs on human skin. The AB(100/79) adhesive maintains strong adhesion under repeated joint movement (e.g., finger and wrist), while the AB(0/78) adhesive exhibits weak adhesion and easily detaches (left). Re-exposure of AB(100/79) adhesive to ethanol vapor enables clean detachment without residue or skin damage (right).

annealing is primarily driven by the dissociation and reformation of H-bonds, with solvent penetration and volatility playing critical roles in modulating adhesion.

Lastly, skin adhesion tests were conducted during joint movements to demonstrate the practical utility of the fabricated PSAs (Figure 9). Medical-grade ethanol was used in all tests to prevent potential skin irritation during solvent vapor annealing. The AB(0/78) sample initially adhered but failed under joint motion, whereas the AB(100/79) sample maintained strong adhesion to highly mobile areas, such as the fingers and wrists, without detachment (Movie S3, Supporting Information). Furthermore, using ethanol vapor enabled easy removal without causing skin damage (Movie S4, Supporting Information).

3. Conclusion

In summary, a series of supramolecular LCEs were synthesized to investigate the effects of internal damping and H-bonding interactions on viscoelastic response, soft elasticity, and adhesion. Decreasing the LC content in LCEs reduced internal damping and soft elasticity, resulting in lower adhesion strength. Introducing H-bonds through rigid non-mesogenic comonomers restricted mesogen reorientation and suppressed adhesion. In contrast, incorporating H-bonds into flexible chain segments while maintaining a high LC content enhanced internal dissipation, soft elasticity, and adhesion. Thus, the adhesion performance of supramolecular LCEs was primarily governed by internal damping rather than by H-bonding interactions. Finally, solvent vapor annealing provided a non-thermal strategy to re-

versibly control adhesion strength by temporarily weakening and reforming H-bonds without inducing phase transitions. Therefore, supramolecular LCEs enable solvent-triggered reversible adhesion without disrupting the LC phase, offering a promising strategy for thermally sensitive applications, such as medical patches. Future studies focusing on solvent quality and different H-bonding moieties may further broaden the functionality and application potential of supramolecular LCE adhesives.

4. Experimental Section

Materials: The LC monomer 1,4-bis-[4-(6-acryloyloxyhexyloxy)benzoyloxy]-2-methylbenzene (RM82) was purchased from Daken Chemicals. The isotropic monomers, Bisphenol A ethoxylate diacrylate (BE) and Bisphenol A glycerolate (1 glycerol/phenol) diacrylate (BG) were obtained from Sigma-Aldrich. The amine chain extenders *n*-hexylamine and 4-Amino-1-butanol (AB) were purchased from Thermo Fisher Scientific and TCI, respectively. The vinyl crosslinker 1,3,5-triazine-2,4,6-(1H,3H,5H)-trione (TATATO) and antioxidant 2,6-di-*tert*-butyl-4-methylphenol (BHT) were purchased from Sigma-Aldrich. The photoinitiator Irgacure-369 (I-369) was donated by the BASF Corporation. All the materials were used without further purification.

Preparation of PSA Series: All acrylate-terminated oligomers were synthesized via an aza-Michael addition reaction. A non-equimolar mixture of the diacrylate monomer and amine chain extender was dissolved in DMF, with BHT added as an antioxidant. The mixture was homogenized using a heat gun and then oligomerized for 21 h in a convection oven at 65 °C to form the acrylate-terminated oligomer. The resulting oligomers were mixed with TATATO and I-369. The molar ratio was adjusted to 1.01 (acrylate): 1 (amine): 0.3 (vinyl), with the amounts of BHT and I-369 set to 1.5 wt.% of the total mixture. The representative AB(100/79) oligomer

was synthesized using RM82 (600 mg, 0.89 mmol), 4-amino-1-butanol (79 mg, 0.88 mmol), TATATO (66 mg, 0.26 mmol), BHT (11.3 mg), and I-369 (11.3 mg). In all samples, LC monomer amount was fixed at 600 mg, and DMF was added at 0.7 mL per 600 mg of LC monomer for dissolution.

To fabricate the adhesive, the oligomers were cast onto a PET backing film using a tape-casting coater (MSK-AFA-II-VC, MTI Corporation). Before coating, the PET film was treated with O₂ plasma using a plasma cleaner (Harrick PDC-32G; Harrick Plasma) to ensure strong bonding with the oligomer. During coating, an applicator with a 500 µm gap was used at a speed of 5 mm s⁻¹ at 80 °C. The coated oligomer was dried for 3 h at 150 °C to remove any residual solvent. Finally, the coated oligomers were exposed to UV light at room temperature for 30 min to induce crosslinking. The final thickness of the adhesive was 200 µm.

Material Characterization: DSC was conducted using a Discovery DSC25 (TA Instruments) under nitrogen flow. The adhesive films underwent a heating-cooling-heating cycle. They were first heated to 150 °C, cooled to -50 °C, and then reheated to 150 °C at a rate of 10 °C min⁻¹. FT-IR spectra were recorded in the 4000–400 cm⁻¹ wavelength range using a Jasco FTIR-4600 spectrometer in transmission mode. A background spectrum (32 scans at 4 cm⁻¹ resolution) of an empty sample holder was obtained and used as a reference. Temperature-dependent real-time FT-IR spectra were measured in the transmission mode using a heating stage (Linkam LTS420). Specifically, the adhesive films were placed on a sample holder, and the O–H stretching peak was monitored during heating. The temperature of the heating stage was calibrated using an infrared camera (FLIR, E5-XT).

Thermomechanical, iso-stress, and frequency sweep measurements were conducted using a dynamic mechanical analyzer (DMA Q850, TA Instruments) equipped with a tensile clamp. For all measurements, the adhesive films were cut into rectangles (7 mm (L) × 5 mm (W) × 0.2 mm (T)). Viscoelastic measurements were performed from -50 to 150 °C at a rate of 3 °C min⁻¹ under a constant frequency of 1 Hz. Iso-stress experiments were performed under a constant tensile stress of 0.1 MPa. During testing, the sample was heated from 0 to 200 °C at a rate of 3 °C min⁻¹. The corresponding change in sample length was recorded throughout the heating process. The frequency sweep test was conducted from 0.1 to 100 Hz under a constant strain of 0.2% at 25 °C.

Gel Fraction: The adhesive films were immersed in DMF for 48 h at room temperature to extract uncrosslinked segments. Subsequently, the samples were dried in a vacuum oven for 48 h at room temperature, followed by an additional 3 h at 80 °C. The mass of each sample was measured before and after extraction, with the gel fraction (G) calculated using the following equation:

$$G (\%) = \frac{m_f}{m_i} \times 100 (\%) \quad (2)$$

where m_i is the initial mass of the sample before immersion and m_f is the mass of the dried sample after extraction.

Uniaxial Tensile Test: Stress-strain measurements were performed on a universal testing machine (DR TECH, DR-100) using the rectangular films (7 mm (L) × 5 mm (W) × 0.2 mm (T)) at an elongation rate of 100 mm min⁻¹ at room temperature. To quantify soft elasticity, the stress plateau region was defined between 25% and 50% strain, where deformation occurred with a minimal increase in stress owing to mesogen rotation. The soft elasticity value was calculated as the slope of the stress-strain curve in this region using the following equation:

$$\text{Soft elasticity (MPa)} = \frac{\sigma_{\epsilon=50\%} - \sigma_{\epsilon=25\%}}{\epsilon_{50\%} - \epsilon_{25\%}} \quad (3)$$

where $\sigma_{\epsilon=25\%}$ and $\sigma_{\epsilon=50\%}$ are the stress values at 25% and 50% strain, respectively. A lower slope indicates a more pronounced soft elastic response, characteristic of LCE network deformation.

180° Peel Test: Peel tests were conducted using a dynamic mechanical analyzer (DMA Q850, TA Instruments) in the tensile mode. The adhesives attached to a PET backing film were mounted onto a glass substrate, with the glass substrate secured to the top-fixed clamp. Then, the

bottom-moving clamp was peeled the adhesives at a constant rate of 100 mm min⁻¹. Before testing, all samples were equilibrated at a specific temperature for 3 min. The peel force measurements were normalized to the adhesive width (10 mm). To investigate the temperature dependency of the adhesives, peel forces were recorded at temperatures ranging from 65 to 150 °C. Prior to testing, all samples were equilibrated at each measurement temperature for 3 min.

Solvent Vapor Annealing: All adhesives were suspended in a 250 mL beaker containing ≈150 mL of ethanol. The adhesives were positioned ≈10 mm above the solvent surface using a metal clip. The beaker was sealed and maintained at room temperature to establish a stable ethanol vapor environment. It was ensured that the PSAs did not come into direct contact with the liquid ethanol. Following exposure, the samples were transferred to a vacuum oven and dried for 1 h at 40 °C to facilitate H-bonding restoration and network structure stabilization.

Supporting Information

Supporting Information is available from the Wiley Online Library or from the author.

Acknowledgements

This work was supported by the National Research Foundation of Korea (NRF) grants funded by the Ministry of Science and ICT (MSIT) of the Korean Government (RS-2023-00208130 and RS-2023-00221396). We thank Y. Choi for her experimental support.

Conflict of Interest

The authors declare no conflict of interest.

Data Availability Statement

The data that support the findings of this study are available from the corresponding author upon reasonable request.

Keywords

adhesion, damping, liquid crystal elastomers, pressure sensitive adhesives, solvent vapor annealing

Received: May 7, 2025

Revised: June 12, 2025

Published online:

- [1] C. Creton, *MRS Bull.* **2003**, 28, 434.
- [2] X. He, W. Wang, S. Yang, F. Zhang, Z. Gu, B. Dai, T. Xu, Y. Y. S. Huang, X. Zhang, *Appl. Phys. Rev.* **2023**, 10, 011305.
- [3] C. A. Dahlquist, *Treatise on Adhesion and Adhesives*, 2, Marcel Dekker, New York **1969**, 219.
- [4] E. P. Chang, *J. Adhes.* **1997**, 60, 233.
- [5] T. Ohzono, M. O. Saed, E. M. Terentjev, *Adv. Mater.* **2019**, 31, 1902642.
- [6] T. Ohzono, Y. Norikane, M. O. Saed, E. M. Terentjev, *ACS Appl. Mater. Interfaces* **2020**, 12, 31992.
- [7] H. J. Farre-Kaga, M. O. Saed, E. M. Terentjev, *Adv. Funct. Mater.* **2022**, 32, 2110190.

- [8] H. Guo, M. O. Saed, E. M. Terentjev, *Macromolecules* **2023**, *56*, 6247.
- [9] R. Annappooranan, S. Suresh Jeyakumar, R. J. Chambers, R. Long, S. Cai, *Adv. Funct. Mater.* **2024**, *34*, 2309123.
- [10] P. A. Pranda, A. Hedegaard, H. Kim, J. Clapper, E. Nelson, L. Hines, R. C. Hayward, T. J. White, *ACS Appl. Mater. Interfaces* **2024**, *16*, 6394.
- [11] R. Annappooranan, R. H. Yeerella, R. J. Chambers, C. Li, S. Cai, *Proc. Natl. Acad. Sci. USA* **2024**, *121*, 2412635121.
- [12] H. Gou, S. Hou, M. O. Saed, *Adv. Mater. Interfaces* **2024**, *11*, 2400488.
- [13] S. Choi, H. Guo, B. Kim, J.-H. Seo, E. M. Terentjev, M. O. Saed, S.-k. Ahn, *Adv. Funct. Mater.* **2025**, *35*, 2413824.
- [14] T. Ohzono, H. Minamikawa, E. Koyama, Y. Norikane, *Adv. Mater. Interfaces* **2021**, *8*, 2100672.
- [15] T. Ohzono, H. Minamikawa, E. Koyama, Y. Norikane, *Macromolecules* **2021**, *54*, 8987.
- [16] T. Ohzono, E. Koyama, *Polymer* **2022**, *260*, 125377.
- [17] S. V. Fridrikh, E. M. Terentjev, *Phys. Rev. E* **1999**, *60*, 1847.
- [18] M. Warner, P. Bladon, E. M. Terentjev, *J. Phys. II France* **1994**, *4*, 93.
- [19] S. Dey, D. M. Agra-Kooijman, W. Ren, P. J. McMullan, A. C. Griffin, S. Kumar, *Crystals* **2013**, *3*, 363.
- [20] K. M. Herbert, H. E. Fowler, J. M. McCracken, K. R. Schlafmann, J. A. Koch, T. J. White, *Nat. Rev. Mater.* **2022**, *7*, 23.
- [21] T. J. White, D. J. Broer, *Nat. Mater.* **2015**, *14*, 1087.
- [22] E. M. Terentjev, *Macromolecules* **2025**, *58*, 2792.
- [23] S. M. Clarke, A. R. Tajbakhsh, E. M. Terentjev, C. Remillat, G. R. Tomlinson, J. R. House, *J. Appl. Phys.* **2001**, *89*, 6530.
- [24] N. A. Traugutt, R. H. Volpe, M. S. Bollinger, M. O. Saed, A. H. Torbati, K. Yu, N. Dadivanyan, C. M. Yakacki, *Soft Matter* **2017**, *13*, 7013.
- [25] D. Mistry, N. A. Traugutt, B. Sanborn, R. H. Volpe, L. S. Chatham, R. Zhou, B. Song, K. Yu, K. N. Long, C. M. Yakacki, *Nat. Commun.* **2021**, *12*, 6677.
- [26] Y. Lee, S. Choi, B.-G. Kang, S.-k. Ahn, *Materials* **2020**, *13*, 3094.
- [27] S. Choi, B. Kim, S. Park, J.-H. Seo, S.-k. Ahn, *ACS Appl. Mater. Interfaces* **2022**, *14*, 32486.
- [28] M. O. Saed, W. Elmadih, A. Terentjev, D. Chronopoulos, D. Williamson, E. M. Terentjev, *Nat. Commun.* **2021**, *12*, 6676.
- [29] S.-k. Ahn, P. Deshmukh, M. Gopinadhan, C. O. Osuji, R. M. Kasi, *ACS Nano* **2011**, *5*, 3085.
- [30] S. Chen, Z. Li, Y. Wu, N. Mahmood, F. Lortie, J. Bernard, W. H. Binder, J. Zhu, *Angew. Chem., Int. Ed.* **2022**, *61*, 202203876.
- [31] N. Jimenez, N. Ballard, J. M. Asua, *Polymer* **2021**, *233*, 124210.
- [32] S. Chen, K. Zhang, Z. Li, Y. Wu, B. Zhu, J. Zhu, *Supramol. Mater.* **2023**, *2*, 100032.
- [33] D. Thomas, C. Matt, S.-F. Antoni, B. L. Mbanga, T. J. Atherton, P. Cebe, *Liq. Cryst.* **2015**, *43*, 112.
- [34] Y. Zhan, D. J. Broer, J. Li, J. Xue, D. Liu, *Mater. Horiz* **2023**, *10*, 2649.
- [35] E. Wittenberg, A. Meyer, S. Eggers, V. Abetz, *Soft Matter* **2018**, *14*, 2701.
- [36] R. Nasare, H. Guo, A. Priimagi, *J. Mater. Chem. B* **2025**, *13*, 1704.
- [37] A. Gasperini, G.-J. N. Wang, F. Molina-Lopez, H.-C. Wu, J. Lopez, J. Xu, S. Luo, D. Zhou, G. Xue, J. B. H. Tok, Z. Bao, *Macromolecules* **2019**, *52*, 2476.
- [38] B. Liu, X. Chen, G. A. Spiering, R. B. Moore, T. E. Long, *Molecules* **2021**, *26*, 4705.
- [39] R. H. Pritchard, A.-L. Redmann, Z. Pei, Y. Ji, E. M. Terentjev, *Polymer* **2016**, *95*, 45.
- [40] Q. Chen, W. Li, Y. Wei, Y. Ji, *Adv. Intell. Syst.* **2021**, *3*, 2000249.
- [41] J.-H. Lee, J. Bae, J. H. Hwang, M.-Y. Choi, Y. S. Kim, S. Park, J.-H. Na, D.-G. Kim, S.-k. Ahn, *Adv. Funct. Mater.* **2022**, *32*, 2110360.
- [42] G. A. Shandryuk, S. A. Kuptsov, A. M. Shatalova, N. A. Plate, R. V. Talroze, *Macromolecules* **2003**, *36*, 3417.
- [43] H.-H. Yoon, D.-Y. Kim, K.-U. Jeong, S.-k. Ahn, *Macromolecules* **2018**, *51*, 1141.
- [44] Y. Wu, B. D. Clarke, K. M. Liechti, Z. A. Page, *Chem. Mater.* **2024**, *36*, 8066.
- [45] C. Sinturel, M. Vayer, M. Morris, M. A. Hillmyer, *Macromolecules* **2013**, *46*, 5399.
- [46] Y. Cun, C. Song, H. Zheng, J. Wang, C. Mai, Y. Liu, J. Li, D. Yu, J. Wang, L. Ying, J. Peng, Y. Cao, *J. Mater. Chem. C* **2019**, *7*, 4784.
- [47] S. A. H. Jansen, E. Weyandt, T. Aoki, T. Akiyama, Y. Itoh, G. Vantomme, T. Aida, E. W. Meijer, *J. Am. Chem. Soc.* **2023**, *145*, 4231.